Crystal Structures and Phase Transitions in A-Site Deficient Perovskites $Ln_{1/3}TaO_3$

Qingdi Zhou, Paul J. Saines, Neeraj Sharma, Jimmy Ting, and Brendan J. Kennedy*

School of Chemistry, The University of Sydney, Sydney, NSW 2006, Australia

Zhaoming Zhang

Institute of Materials Engineering, Australian Nuclear Science and Technology Organisation, Lucas Heights, NSW 2234, Australia

Ray L. Withers

Research School of Chemistry, The Australian National University, Canberra, ACT 0200, Australia

Kia S. Wallwork

Australian Synchrotron, 800 Blackburn Road, Clayton, VIC 3168, Australia

Received June 5, 2008. Revised Manuscript Received July 28, 2008

The synthesis and structures of the perovskites $Ln_{1/3}TaO_3$ are described. As the size of the Ln cation is reduced, the compounds display a sequence of structure: *P*4/*mmm*/La → *Cmmm*/Ce−Gd → *Pmma*/Tb, Dy → *Pmc*2_1/Ho, Er. Although apparently tetragonal in *P*4/*mmm*, electron diffraction patterns of $Tm_{1/3}TaO_3$ reveal this has a complex incommensurate structure. Likewise $Gd_{1/3}TaO_3$ appears metrically tetragonal, but electron diffraction and synchrotron X-ray powder diffraction demonstrate this is actually orthorhombic. The suppression of the spontaneous orthorhombic strain in $Gd_{1/3}TaO_3$ is thought to be due to the proximity to the first-order *Cmmm*−*Pmma* transition. Variable temperature studies show both $Tb_{1/3}TaO_3$ and $Dy_{1/3}TaO_3$ undergo a first-order *Cmmm*−*Pmma* transition upon heating.

Introduction

The perovskite structure is pervasive in solid-state chemistry, and there are numerous commercial applications, ranging from sensors and catalysts to electronic and magnetic materials, that utilize perovskite-type oxides. The ubiquitous nature of the perovskite structure is testament to its enormous structural and compositional flexibility. This flexibility allows perovskite-type oxides to be tuned to near an appropriate instability, be it structural, electronic, or magnetic in origin, which is essential for the oxide to be functionally useful. Perovskites are also of enormous importance in the geosciences. Consequently, establishing both the precise structure of a specific perovskite-type oxide and its response to an external stimulus such as temperature or pressure is of both fundamental and practical importance.

It is over 40 years since Rooksby et al.[1] and Keller and Walter[2] simultaneously reported systematic studies of the synthesis and structures of the A-site deficient tantalum perovskite oxides $Ln_{1/3}TaO_3$ where Ln = La, Ce, ..., Yb. The stoichiometry of these oxides is described by some as $LnTa_3O_9$, although the relationship to the ABO_3 perovskite structure is less obvious from this latter description. Shortly afterward Iyer and Smith[3] used a combination of single-crystal and powder diffraction methods to describe the structures of the same series. Although the resolution of the diffractometer was moderate by modern standards, the study by Rooksby et al.[1] suggests a lowering of symmetry from tetragonal to orthorhombic and finally monoclinic as the size of the trivalent lanthanide decreased across the series. A notable exception was the structures of $Nd_{1/3}TaO_3$ and $Sm_{1/3}TaO_3$ which were described as tetragonal (when expected to be orthorhombic based on the Ln size). In contrast, the studies by Keller and Walter[2] and by Iyer and Smith[3] concluded that the symmetry was first lowered from tetragonal to orthorhombic but then back to tetragonal as the size of the lanthanide decreased. In 2000 Ebisu et al.[4] revisited the series, and although they also reported tetragonal, orthorhombic, and monoclinic structures, the structural sequence was tetragonal (Ln = La) → orthorhombic (Ln = Ce−Eu) → tetragonal (Ln = Gd) → monoclinic (Ln = Tb−Ho) → tetragonal (Ln = Er−Yb) as the ionic radius of the Ln decreased. No structural refinements were carried out in the above-mentioned studies, except for $La_{1/3}TaO_3$, which was tetragonal in *P*4/*mmm* with $a = 3.918$ and $c = 7.913$ Å.[3]

In addition to these four systematic studies several researchers have investigated the structures of selected

* To whom correspondence should be addressed. E-mail: B.Kennedy@chem.usyd.edu.au.

(1) Rooksby, H. P.; White, E. A. D.; Langston, S. A. *J. Am. Ceram. Soc.* **1965**, *48*, 447.
(2) Keller, C.; Walter, K. H. *J. Inorg. Nucl. Chem.* **1965**, *27*, 1247.
(3) Iyer, P. N.; Smith, A. J. *Acta Crystallogr.* **1967**, *23*, 740.
(4) Ebisu, S.; Morita, H.; Nagata, S. *J. Phys. Chem. Solids* **2000**, *61*, 45.

10.1021/cm8014868 CCC: $40.75
Published on Web 10/15/2008

examples in the series $Ln_{1/3}TaO_3$ but with conflicting conclusions. For example, Yamnova et al.[5] reported that $Nd_{1/3}TaO_3$ was tetragonal in *P*4/*mmm* with $a = 3.920$ and $c = 7.791$ Å in contrast to the orthorhombic structure proposed in refs 2−4. Ibarra Polas et al.[6] reported the existence of a continuous solid solution in the series $Tb_{1/3-x}Eu_xTaO_3$ and concluded that the structure evolves from tetragonal in *P*4/*mmm* for $Tb_{1/3}TaO_3$ with $a = 3.860$ and $c = 7.780$ Å to orthorhombic in *Pmmm* for $Eu_{1/3}TaO_3$ with $a = 3.869$, $b = 3.884$, and $c = 7.797$ Å. Although these authors did not explicitly comment on the nature of the transition between these two structures their published results are suggestive of a first-order transition. Ebisu et al.[4] put $Eu_{1/3}TaO_3$ on the same size orthorhombic cell but suggested $Tb_{1/3}TaO_3$ was monoclinic. Komeno et al.[7] used powder neutron diffraction to investigate the structure of $Y_{0.22}(Ta_{0.66}W_{0.34})O_3$ first described by Studer et al.[8] and concluded that this exhibited partial ordering of the Y cations and associated vacancies and that the structure was monoclinic. The details of the structures in the $Ln_{1/3}TaO_3$ series are clearly confusing.

Besides the above-mentioned studies several structures that are not perovskite-like have also been reported for $La_{1/3}TaO_3$,[9] $Ce_{1/3}TaO_3$,[10] $Pr_{1/3}TaO_3$, and $Nd_{1/3}TaO_3$.[11] Evidently, the exact structures of these compounds depended on the detailed conditions used in the sample preparation.

The structure of the $Ln_{1/3}TaO_3$ oxides is derived from the archetypal cubic ABO_3 perovskite with cell doubling along one axis (typically taken to be *z*) due to the layered ordering of the Ln cations and vacancies. In this way one layer contains no A-type, Ln, cations and the other is partially occupied. This ordering of the cations and vacancies results in a tetragonal structure that is in the centrosymmetric space group, *P*4/*mmm*, and has $a = b \sim a_p$ and $c \sim 2a_p$ where a_p is the equivalent primitive cell parameter.[12] This is described as a $1 \times 1 \times 2$ cell. Tilting of the corner-sharing TaO_6 octahedral units relative to each other can occur and further reduces the symmetry. The magnitude of this tilting is expected to increase as the size of the trivalent lanthanide is reduced, and it is not unreasonable to expect a systematic reduction in symmetry across the series of lanthanides. Such a reduction in symmetry appears to be present in the closely related titanates $Ln_{2/3}TiO_3$[12,13] and, in the limited number of examples available, niobates $Ln_{1/3}NbO_3$.[14,15] The published experimental results described above do not, apparently, support this expectation for the tantalates, with a tetragonal structure proposed for the largest (Ln = La), intermediate (e.g., $Gd_{1/3}TaO_3$), and smallest (Ln = Yb or Tm) lanthanides studied.

In addition to the long-standing crystallographic questions regarding the appropriate symmetries for the various members in the $Ln_{1/3}TaO_3$ series, there has been interest in these oxides stemming from their possible use as Li ion electrolytes in high energy density batteries and electrochemical devices. There is also interest in using these oxides as luminescence materials.[16] Imaki et al.[17] have monitored the changes accompanying Li insertion into $Gd_{1/3}TaO_3$ using X-ray diffraction and X-ray absorption spectroscopy. These workers described their structural studies of $Gd_{1/3}TaO_3$ as being consistent with Rooksby et al.[1] and Iyer and Smith[3] concluding that $Gd_{1/3}TaO_3$ is orthorhombic in space group *Pmmm* on a $1 \times 1 \times 2$ cell. This is, however, inconsistent with the results of a group-theoretical analysis by Zhang et al.[12] in which all the possible structures resulting from a combination of cation ordering and octahedral tilting were enumerated. According to their analysis any $A_{1/3}TaO_3$ layered perovskite structure in *Pmmm* has to be on a bigger cell.

Given the potential of these oxides for practical applications and the unexpected, and sometimes conflicting, structures reported it was decided to re-examine this series. The aim of the present work was to establish accurate and precise structures for the members in the series $Ln_{1/3}TaO_3$ with Ln = La−Tm. This has been accomplished using high-resolution synchrotron X-ray powder diffraction and electron microscopy. Variable temperature studies have also been undertaken as required to better understand the transitions between the various structures.

Experimental Section

Polycrystalline samples of 12 members in the series of $Ln_{1/3}TaO_3$ and the solid solution samples of $Tb_{(1-x)/3}Gd_{x/3}TaO_3$ and $Tm_{(1-x)/3}Er_{x/3}TaO_3$ were prepared by the reaction of the appropriate stoichiometric mixture of Ta_2O_5 (Aldrich 99.99% in purity) and Ln_2O_3 (Ln = La, Nd, Sm, Eu, Gd, Dy, Ho, Er, and Tm; Aldrich, 99.9+%), CeO_2 (Aldrich 99.999%), Pr_6O_{11} (Aldrich 99.9%), Tb_4O_7 (Aldrich 99.9%). All lanthanide oxides were preheated at 1000 °C overnight before use. The well-mixed powders were first heated at 850 °C for 12 h, and then at 1450 °C, until a single-phase sample was obtained.

Single crystals of the Gd and Tm tantalates were prepared by combining the appropriate stoichiometric mixtures of Ta_2O_5 (Aldrich 99.99%) and Ln_2O_3 (Ln = Gd, Tm) and heating these for 12 h at 850 °C and 48 h at 1450 °C. The powders of each sample were then fabricated into rods 7 cm long and 0.5 cm diameter by pressing at 60 MPa (Riken hydrostatic press), and the rods were sintered in a vertical tube furnace at 1450 °C with a rotating speed of 10 rpm, while moving five times through the hot zone at a rate of 63.5 mm/min. The rods were then mounted in an optical floating zone furnace (Crystal Systems Corporation model FZ-T-10000-H-

(5) Yamnova, N. A.; Pushcharovsky, D. Y.; Leonyuk, L. I. *Kristallografiya* **1989**, *34*, 1017.
(6) Ibarra Palos, A.; Villafuerte Castrejon, M. E.; Duque, J.; Pomes, R. *J. Solid State Chem.* **1996**, *124*, 272.
(7) Komeno, A.; Aoyama, Y.; Toda, K.; Sato, M.; Uematsu, K. In *Electroceramics in Japan VII*, 2004; Vol. 269, p 11.
(8) Studer, F.; Montfort, Y.; Raveau, B. *J. Solid State Chem.* **1973**, *7*, 269.
(9) Langenbachkuttert, B.; Sturm, J.; Gruehn, R. *Z. Anorg. Allg. Chem.* **1987**, *548*, 33.
(10) Schaffrath, U.; Gruehn, R. *Z. Anorg. Allg. Chem.* **1988**, *565*, 67.
(11) Schaffrath, U.; Steinmann, G.; Gruehn, R. *Z. Anorg. Allg. Chem.* **1988**, *565*, 54.
(12) Zhang, Z. M.; Howard, C. J.; Knight, K. S.; Lumpkin, G. R. *Acta Crystallogr., Sect. B: Struct. Sci.* **2006**, *62*, 60.
(13) Howard, C. J.; Zhang, Z. M. *J. Phys.: Condens. Matter* **2003**, *15*, 4543.
(14) Zhang, Z. M.; Howard, C. J.; Kennedy, B. J.; Knight, K. S.; Zhou, Q. D. *J. Solid State Chem.* **2007**, *180*, 1846.
(15) Kennedy, B. J.; Howard, C. J.; Kubota, Y.; Kato, K. *J. Solid State Chem.* **2004**, *177*, 4552.
(16) Kubota, S.; Endo, T.; Takizawa, H.; Shimada, M. *J. Alloys Compd.* **1994**, *210*, 103.
(17) Imaki, K.; Nakayama, M.; Uchimoto, Y.; Wakihara, M. *Solid State Ionics* **2004**, *172*, 73.

VI-VPM-PC). The counter-rotating rods melted between 80% and 85% power with 500−1500 W filaments.

The sample purity was established through powder X-ray diffraction measurements using Cu Kα radiation on a Shimadzu D-6000 diffractometer. Synchrotron X-ray powder diffraction data were recorded from the single lanthanide containing samples using the Debye−Scherrer diffractometer on beamline 20B, the Australian National Beamline Facility (ANBF), at the Photon Factory, Tsukuba Japan.[18] Data were collected in 0.01° steps over the angular range of $5° \leq 2\theta \leq 85°$ using two image plates as detectors. Each image plate is 20×40 cm^2 and covers 40° in 2θ. The wavelength of the X-rays used was about 0.8 Å, accurately calibrated using Si 640c during each run. The samples were held in 0.3 mm diameter capillaries that rotated throughout the measurements. Temperatures up to 800 °C were achieved using a custom-built furnace. Data were also collected for samples with Ln = Gd and Tm at 90 and 300 K on the Debye−Scherrer diffractometer on BL-02B2 at SPring-8.[19] These data were collected at angles of up to 85° using a single Fuji image plate as the detector with an incident X-ray wavelength of 0.60265(1) Å estimated using CeO_2. The samples were sealed in 0.2 mm diameter glass capillaries and cooled using a liquid nitrogen cryostream with the temperature held to within ±1° of the set point during the measurements.

Diffraction data for $Tb_{(1-x)/3}Gd_{x/3}TaO_3$ and $Tm_{(1-x)/3}Er_{x/3}TaO_3$ were collected at the powder diffraction beamline, 10-BM,[20] at the Australian Synchrotron using the MYTHEN microstrip detector.[21] Samples were loaded into 0.3 mm capillaries and mounted and aligned concentric to the rotation axis of the three-circle diffractometer. The wavelength was refined to 0.80093(1) Å using NIST standard 660a, LaB_6. Data were collected over the range of 3−85°; these data were collected in two frames, shifted by 2.0° in order to cover the small gaps (ca. 0.2°) which are inherent in the detector and occur every 5°. Temperature control was achieved using a liquid nitrogen cryostream.

Structures were refined from the powder diffraction data using the Rietveld method as implemented in the program RIETICA.[22]

Single crystals of the Gd tantalate were analyzed at room temperature on a Bruker-Nonius Apex 2 laboratory X-ray single-crystal diffractometer with Mo Kα ($\lambda = 0.71073$ Å) radiation. Integration of the data sets was undertaken with SAINTPlus,[23] and a multiscan absorption correction was applied. Structural refinements were carried out using the JANA2006[24] software package. Further details are given in Table 1.

Electron Microscopy. Electron diffraction patterns (EDPs) from crushed grains of the single-crystal samples dispersed onto holey carbon-coated copper grids were recorded on a Philips EM 430 transmission electron microscope operating at 300 kV.

Table 1. Single-Crystal Data for $Gd_{1/3}TaO_3$

	$Gd_{1/3}TaO_3$
crystal data	
space group	orthorhombic *Cmmm*
a (Å)	7.7731(1)
b (Å)	7.7621(2)
c (Å)	7.7826(2)
Z	2
temp (K)	293
wavelength (Å)	0.71073
cryst shape	prismatic
size (μm)	134 × 20 × 45
color	transparent colorless
data collection	
instrument	Bruker-Nonius APEX 2
μ (cm^{-1})	557
range for data collection	$4° < \theta < 30°$
no. of reflections	3780
no. of reflections $I > 3\sigma(I)$	2115
no. of unique reflections	437
R_{int} (%)	3.70
refinement	
no. of params	19
R_{obs}/R_{all} (%)	14.46/15.78
wR_{obs}/wR_{all} (%)	18.74/19.07

Results and Discussion

Room-Temperature Structures. The crystalline powdered samples of $Ln_{1/3}TaO_3$ and the solid solution samples of $Tb_{(1-x)/3}Gd_{x/3}TaO_3$ and $Tm_{(1-x)/3}Er_{x/3}TaO_3$ were successfully prepared using the conventional solid-state reaction method at 1450 °C. The conditions to prepare single-phase samples became more difficult as the size of the Ln cation was reduced, and like previous workers[1,3,4] we could not prepare single-phase samples with the two smallest lanthanides Yb and Lu. These were not investigated further. In general, prolonged annealing was necessary to obtain crystalline single-phase samples. All the polycrystalline samples used in this work were furnace-cooled over several hours. We note that Ebisu et al.[4] reported that $Er_{1/3}TaO_3$ can be a mixture of monoclinic and tetragonal depending on thermal history, an observation that they suggested is related to the formation of random vacancies in the (001) plane. It is unclear how random ordering in the plane would alter the structure, with the present oxides all exhibiting long-range vacancy/cation ordering along [001]. Howard et al.[25] have demonstrated that the cation/vacancy ordering in $La_{0.6}Sr_{0.1}TiO_3$ can be removed by quenching this material from high temperatures and that the symmetry of the quenched sample is higher than that of an unquenched sample that retains such ordering.

The approach we have utilized to establish the appropriate space group for the 12 members of the series $Ln_{1/3}TaO_3$ prepared during this work involves examination of the cell metric for the stronger Bragg reflections that correspond to peaks in the ideal cubic aristotype and analysis of the weak superlattice reflections that arise from the A-site cation/vacancy ordering and tilting of the TaO_6 octahedra. The cation/vacancy ordering is described by the transformation according to the irreducible representation (irrep) $X_3^-(k = 0, 0, {}^1/_2)$ of the $Pm\bar{3}m$ aristotype. Out-of-phase [or −ve] tilting

(18) Sabine, T. M.; Kennedy, B. J.; Garrett, R. F.; Foran, G. J.; Cookson, D. J. *J. Appl. Crystallogr.* **1995**, *28*, 513.
(19) Nishibori, E.; Takata, M.; Kato, K.; Sakata, M.; Kubota, Y.; Aoyagi, S.; Kuroiwa, Y.; Yamakata, M.; Ikeda, N. *Nucl. Instrum. Methods Phys. Res., Sect. A* **2001**, *467*, 1045.
(20) Wallwork, K. S.; Kennedy, B. J.; Wang, D. *AIP Conf. Proc.* **2007**, *879*, 879.
(21) Schmitt, B.; Bronnimann, C.; Eikenberry, E. F.; Gozzo, F.; Hormann, C.; Horisberger, R.; Patterson, B. *Nucl. Instrum. Methods Phys. Res., Sect. A* **2003**, *501*, 267.
(22) Hunter, B. A.; Howard, C. J. In *A Computer Program for Rietveld Analysis of X-Ray and Neutron Powder Diffraction Patterns*; Lucas Heights Research Laboratories: Sydney, Australia, 1998; p 1.
(23) SAINTPlus: v. 6.45 Data Reduction and Correction Program; Bruker AXS, 2001.
(24) Petricek, V.; Dusek, M.; Palatinus, L. JANA2006, The Crystallographic Computing System, 2007.
(25) Howard, C. J.; Zhang, Z. M.; Carpenter, M. A.; Knight, K. S. *Phys. Rev. B* **2007**, *76*, 9.

Table 2. Refined Lattice and Positional Parameters for $La_{1/3}TaO_3$ at Room Temperature

atom	site	*x*	*y*	*z*	B_{iso} (Å^3)
Space Group *P4/mmm*, $a = 3.91858(2)$, $c = 7.91320(5)$ Å					
La	1*c*	0.5	0.5	0	0.48(3)
Ta	2*g*	0	0	0.2600(3)	0.49(13)
O1	1*a*	0	0	0	1.04(10)[a]
O2	1*b*	0	0	0.5	1.04(10)[a]
O3	4*i*	0	0.5	0.2325(13)	1.04(10)[a]

[a] The displacement parameters for the three crystallographically unique anions were restrained to be equal.

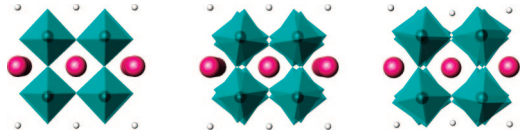

Figure 1. Representations of the tetragonal *P4/mmm* and orthorhombic *Cmmm* and *Pmma* structures observed at room temperature in $La_{1/3}TaO_3$, $Ce_{1/3}TaO_3$, and $Tb_{1/3}TaO_3$, respectively. The TaO_6 are shown as octahedra, the Ta atom being visible within them; the bigger spheres outside these octahedra represent Ln^{3+} cations in the partly occupied layer, and the smaller spheres represent the A-site vacancies. The figures are a perspective view along the *x*-axis. The movements of O^{2-} and Ta^{5+} ions, respectively, toward and away from the partially occupied Ln layers result in a discernible offset of the Ta atom.

of the TaO_6 octahedra is represented through the irrep $R_4^+(k = {}^1/_2, {}^1/_2, {}^1/_2)$ and in-phase [or +ve] tilting through $M_3^+(k = {}^1/_2, {}^1/_2, 0)$. The additional Bragg reflections are labeled *X*-point, *R*-point or *M*-point reflections reflecting the irrep associated with their appearance. *M*-point reflections can also occur due to *X*- and *R*-point distortions acting in concert.[26]

The synchrotron X-ray diffraction pattern of $La_{1/3}TaO_3$ could be indexed to a tetragonal $1 \times 1 \times 2$ cell with only *X*-point superlattice reflections evident, suggesting *P4/mmm* is appropriate. Refinement of a structure in this space group using the model described by Iyer and Smith[3] was uneventful, and the refined parameters are listed in Table 2. In this structure the Ta^{5+} cations are displaced away from the partially occupied La^{3+} layer to give one long and one short Ta−O bond, see Figure 1.

For $Ce_{1/3}TaO_3$ the cell metric is orthorhombic suggesting tilting of the TaO_6 octahedra has occurred to lower the symmetry. The orthorhombic structure is readily observed by the splitting of the 200 reflection (index based on the *P4/mmm* tetragonal cell) near $2\theta \approx 23.5°$ ($d \approx 1.95$ Å) as illustrated in Figure 2. Close scrutiny of the diffraction profile did not reveal any evidence for *R*-point or *M*-point reflections arising from octahedral tilting; however, this is thought to reflect the presence of the very heavy Ce and Ta oxides, rather than demonstrating the absence of any tilting. A combination of powder neutron and X-ray diffraction data has shown that the structure of the closely related Nb oxide $La_{1/3}NbO_3$ is in *Cmmm*.[15] Given the similarity in the chemistry of Nb^{5+} and Ta^{5+} we elected to use the same orthorhombic space group, *Cmmm*, to refine the structure of $Ce_{1/3}TaO_3$. This is characterized by A-site cation/vacancy ordering along the *z*-axis and out-of-phase TaO_6 octahedral tilting around the *x*-axis, perpendicular to the ordering

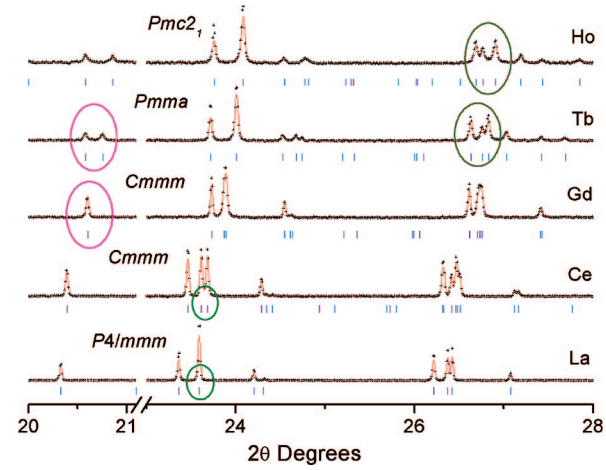

Figure 2. Portions of the synchrotron diffraction patterns for representative members in the series $Ln_{1/3}TaO_6$. The data were collected with $\lambda = 0.80073$ Å at the ANBF. The circles highlight the reflections most sensitive to changes in symmetry.

direction, see Figure 1. In Glazer[27] notation this is $a^-b^0c^0$. This model provided an excellent fit to the data. Again we observe the Ta cations are displaced toward the occupied Ln layer, resulting in one long and one short Ta−O bond. This space group also proved satisfactory for the four oxides with Ln = Pr, Nd, Sm, and Eu. A medium resolution neutron diffraction pattern collected for $Pr_{1/3}TaO_3$ showed strong *R*-point reflections associated with the TaO_6 tilting verifying the appropriateness of this model. The apparent orthorhombic distortion increased from $Ce_{1/3}TaO_3$ to $Nd_{1/3}TaO_3$ (see Table 3) presumably due to the progressive reduction in the size of the trivalent lanthanide cation and the consequent decrease in the Goldschmidt tolerance factor *t*; $t = (r_A + r_O)/\sqrt{2}(r_B + r_O)$. However, distortion decreased with a further reduction in the lanthanide size from Nd to Eu, the origin of which is unclear.

The diffraction pattern of $Gd_{1/3}TaO_3$ appears simpler than that of $Ce_{1/3}TaO_3$ (and the other orthorhombic oxides with Ln = Ce−Eu) (see Figure 2), and the majority of the peaks could be indexed to a tetragonal cell. The fit to the data in *P4/mmm* was satisfactory with $R_p = 4.35\%$ and $R_{wp} = 6.21\%$. The fit in *Cmmm* was, however, noticeably better ($R_p = 3.66\%$ and $R_{wp} = 5.20\%$) with a very small orthorhombic distortion $a = 7.71199(5)$, $b = 7.70251(5)$, $c = 7.75730(3)$ Å (Figure 3). The *Cmmm* model accounted for the observed peak broadening of the 004/040 reflections near $2\theta \approx 23.5°$ ($d \approx 1.95$ Å at $\lambda = 0.80073$ Å) as shown in Figure 2, as well as some of the higher angle peaks, Figure 3. Furthermore in the higher quality diffraction data collected at SPring-8 there was evidence for a weak *M*-point reflection, the 112 reflection near $d = 3.165$ Å ($2\theta \approx 10.9°$ at $\lambda = 0.60265$ Å), suggesting tilting of the octahedra persisted in this structure. Unfortunately the strongest *R*-point reflections, the 113/131/311 near $d \approx 2.32$ Å ($2\theta \approx 14.84°$ at $\lambda = 0.60265$ Å, were masked by a weak broad reflection from an unidentified impurity. As noted above, in these layered perovskites *M*-point reflections can arise from the *X*- and *R*-point distortions acting in concert. We postulate that the observa-

(26) Woodward, D. I.; Reaney, I. M. *Acta Crystallogr., Sect. B: Struct. Sci.* **2005**, *61*, 367.

(27) Glazer, A. M. *Acta Crystallogr., Sect. B: Struct. Sci.* **1972**, *B 28*, 3384.

Table 3. Summary of the Space Groups and Lattice Parameters for the Series $Ln_{1/3}TaO_3$ and Measures of the Orthorhombic and Tetragonal Distortions

compd	ionic radii[a]	space group	*a* (Å)	*b* (Å)	*c* (Å)	γ (deg)	vol (Å^3)	ε_{tet}[b]	ε_{ortho}[c]
$La_{1/3}TaO_3$	1.160	*P4/mmm*	3.91858(2)		7.91320(5)	90	121.51(1)	0.00483	0
$Ce_{1/3}TaO_3$	1.14	*Cmmm*	7.83019(5)	7.80769(5)	7.87930(5)	90	481.71(1)	0.00385	0.00143
$Pr_{1/3}TaO_3$	1.126	*Cmmm*	7.82781(6)	7.78882(6)	7.85469(6)	90	478.90(1)	0.00296	0.0025
$Nd_{1/3}TaO_3$	1.109	*Cmmm*	7.81968(6)	7.77320(5)	7.83508(7)	90	476.25(1)	0.00247	0.00298
$Sm_{1/3}TaO_3$	1.079	*Cmmm*	7.79301(7)	7.74820(7)	7.80662(7)	90	471.38(1)	0.00231	0.00289
$Eu_{1/3}TaO_3$	1.066	*Cmmm*	7.77801(8)	7.73869(7)	7.79669(8)	90	469.30(1)	0.00247	0.00254
$Gd_{1/3}TaO_3$	1.053	*Cmmm*	7.74592(7)	7.73841(7)	7.79172(7)	90	467.04(1)	0.00318	5.03856×10^{-4}
$Tb_{1/3}TaO_3$	1.040	*Pbmm*[d]	5.47920(7)	5.41150(6)	7.79351(9)	90	231.08(1)	0.00598	−0.00623
$Dy_{1/3}TaO_3$	1.027	*Pbmm*	5.47790(6)	5.38971(6)	7.78390(8)	90	229.81(1)	0.00646	−0.00802
$Ho_{1/3}TaO_3$	1.015	$P2_1am$[d]	5.47550(12)	5.37044(12)	7.77129(17)	90	228.52(1)	0.00661	−0.00969
$Er_{1/3}TaO_3$	1.004	$P2_1am$	5.47391(9)	5.35349(9)	7.76061(2)	90	227.42(1)	0.00677	−0.0111
$Tm_{1/3}TaO_3$	0.994	*P4/mmm*	3.83091(4)		7.74370(8)	90	113.65(1)	0.00536	0

[a] Ref 30. [b] $\varepsilon_{tet} = [c_p - 1/2(a_p + b_p)]/[c_p + 1/2(a_p + b_p)]$. [c] $\varepsilon_{ortho} = (a_p - b_p)/(a_p + b_p)$. [d] Results are presented in the nonstandard settings to allow easy comparison between structures.

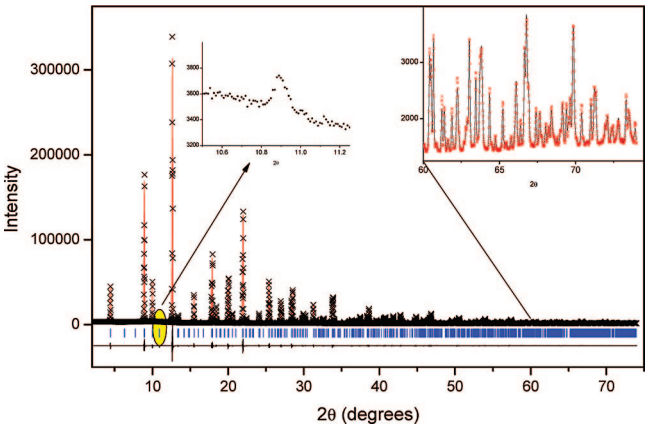

Figure 3. Rietveld plot for $Gd_{1/3}TaO_3$ fitted in *Cmmm*. The crosses represent the observed data, and the solid line joining them is the calculated profile. The insets highlight the presence of a weak *M*-point reflection indicative of octahedral tilting and the quality of the data to high angles. The data were collected with $\lambda = 0.60265$ Å at SPring-8. The intensity of the *M*-point 112 reflection near 10.9° is ~0.05% that of the strongest 022 reflection near 12.6°.

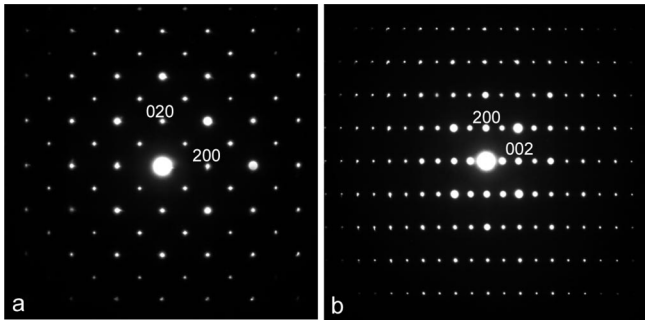

Figure 4. Electron diffraction pattern of (a) a [001] zone axis and (b) a [100] or [010] zone axis for $Gd_{1/3}TaO_3$.

tion of the 112 reflection in the X-ray diffraction pattern occurs through such a mechanism rather than the onset of in-phase tilts of the octahedra. Unfortunately, due to absorption it is not feasible to verify this using neutron diffraction. Rather we sought to confirm this using electron diffraction.

Figure 4 shows the two distinct types of $\langle 001 \rangle_p$ zone axis EDPs typical of $Gd_{1/3}TaO_3$. The first, see Figure 4a, can be unambiguously indexed as a [001] zone axis EDP with respect to the above $2 \times 2 \times 2$ supercell. It shows the characteristic extinction condition $F(hk0) = 0$ unless $h + k$ is even. The second, see Figure 4b, could be indexed as either a [100] or a [010] zone axis EDP, i.e., with the resolution typical of a selected area EDP it is not possible to tell whether the reflection labeled 200 in Figure 4b should be labeled 200 or 020. Given that only two distinct types of $\langle 001 \rangle_p$ zone axis EDPs are ever observed, it seems highly likely that [100] and [010] zone axis EDPs look essentially identical and as shown in Figure 4b. The corresponding extinction conditions $F(h0l) = 0$ unless h is even and $F(0kl) = 0$ unless k is even in conjunction with Figure 4a suggest strongly that the relevant space group symmetry is *Cmmm*. Figure 5 shows a typical $[3,\bar{1},0]$ zone axis EDP showing extended diffuse streaking along c^* running through the $\mathbf{G} \pm {}^1/_2[111]_p^*$ and $\mathbf{G} \pm {}^1/_2[110]_p^*$ type satellite reflections (such as [131]* and [130]* in Figure 5) but not the parent perovskite substructure reflections (**G**) or the $\mathbf{G} \pm {}^1/_2[001]_p^*$ satellite reflections (such as [003]* in Figure 5). Such streaking is indicative of stacking fault disorder perpendicular to $\boldsymbol{c}$ of the $\mathbf{q} = {}^1/_2[111]_p^*$ octahedral rotation mode. In our study[14] of the closely related oxide $Nd_{1/3}NbO_3$ we observed, by high-resolution neutron diffraction, considerable broadening of the *R*-point reflections near the transition to tetragonal, an observation that was attributed to the onset of extensive local disorder associated with and/or impacting on the octahedral tilting.

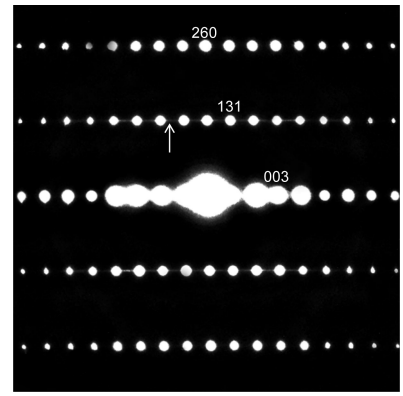

Figure 5. Electron diffraction pattern of a $[3\bar{1}0]$ zone axis for $Ga_{1/3}TaO_3$ illustrating diffuse streaking along the c^* direction indicative of local disorder.

The X-ray diffraction pattern from a single crystal of $Gd_{1/3}TaO_3$ shows the 311 and 131 (in *Cmmm* symmetry) reflections that are not allowed in *P4/mmm*. This corroborates

Table 4. Final Refined Atomic Positions, Occupancy, and Isotropic Displacements Parameters for $Gd_{1/3}TaO_3$ from Single-Crystal and Synchrotron X-ray Diffraction at Room Temperature[a]

atom	site	*x*	*y*	*z*	B_{iso} (Å^3)
		$a = 7.7731(1)$, $b = 7.7621(2)$, $c = 7.826(2)$, Å			
		$a = 7.74611(4)$, $b = 7.73647(4)$, $c = 7.79151(3)$, Å			
Gd	4*g*	0	0.2551(4)	0	1.69(9)
			0.2507(10)		1.00(1)
Ta	8*n*	0.2501(1)	0	0.2567(1)	0.26(6)
		0.2500(2)		0.2593(1)	0.68(1)
O1	4*i*	0.275(9)	0	0	7(2)
		0.2706(44)			3.5(4)
O2	4*j*	0.278(18)	0	0.5	14(2)
		0.2850(20)			1.2(3)
O3	4*k*	0	0	0.261(4)	3(2)
				0.2562(30)	2.5(6)
O4	4*l*	0	0.5	0.241(4)	3(2)
				0.2441(38)	1.5(5)
O5	8*m*	0.25	0.25	0.253(4)	5(3)
				0.2150(26)	6.1(4)

[a] In all cases the lower figure is obtained from the analysis of the synchrotron powder diffraction data.

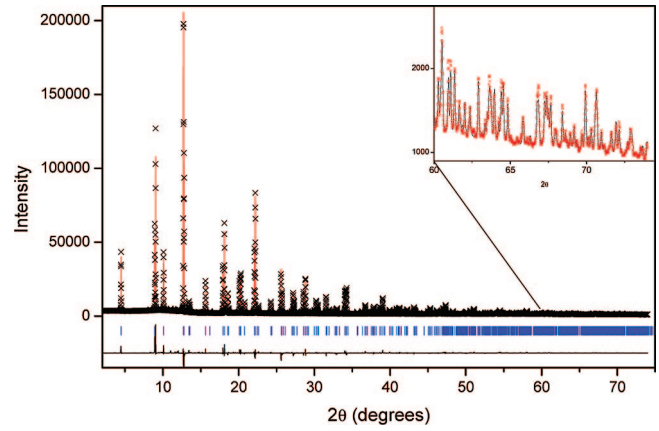

Figure 6. Rietveld plot for $Tm_{1/3}TaO_3$ fitted in *P*4/*mmm*. The crosses represent the observed data, and the solid line joining them is the calculated profile. The inset highlights the quality of the data to high angles. The data were collected with $\lambda = 0.60265$ Å at SPring-8.

evidence provided by the powder and electron diffraction data for *Cmmm* symmetry. The anisotropic shape of the crystal (Table 1), limited number of parameters, and inherent difficulty in refining oxygen parameters in the presence of metals with large X-ray scattering factors result in larger than expected *R* factors. Nevertheless the refinement confirms the orthorhombic symmetry and provides a reasonable description of the structure, Table 4.

The X-ray diffraction pattern for $Tb_{1/3}TaO_3$ was also orthorhombic, but now it could be indexed to a smaller $\sqrt{2} \times 2 \times \sqrt{2}$ cell, and the appropriate space group was *Pmma*. In the standard setting of *Pmma* the ordering axis is defined as the *b*-axis. To facilitate easy comparison with the parent tetragonal cell this should be transformed to a nonstandard setting in *Pbmm*. The *Pbmm* cell accounted for the observed splitting of the *P*4/*mmm* 112 reflections ($2\theta \approx 20.6°$) that remains a singlet in *Cmmm* (see Figure 2). In this structure the A-site cation/vacancy ordering along the *z*-axis persists, but now the out-of-phase tilting is about [110] with the tilt system being $a^-a^-c^0$, Figure 1. The synchrotron diffraction pattern for this showed weak *R*- and *M*-point reflections, in addition to the stronger *X*-point reflections associated with cation ordering. The *M*-point reflections were noticeably weaker than the *R*-point reflections, and it is believed that these arise due to coupling of the *R*- and *X*-point modes.

As the size of the Ln cation was further reduced going from Dy to Ho and ultimately Er, neutron diffraction shows the presence of both *R*- and *M*-point reflections indicating the space group to be $Pmc2_1$. Again we note that the standard setting has *b* as the long (ordering axis), and comparison of the structures is best accomplished in the nonstandard setting where the *c*-axis is unique, namely, of $P2_1am$. The $Pmc2_1$ structure differs from that in *Pbmm* in that it has an additional in-phase tilt about [001]; the tilt system is $a^-a^-c^+$.

The final sample studied was $Tm_{1/3}TaO_3$. We note at the outset that despite repeated efforts we were unable to prepare a high-quality single-phase sample of this oxide. The best samples always contained a number of very weak peaks that could not be indexed to any of the cells described by Zhang et al.[12] The strongest of these peaks was less than 0.75% of the intensity of the strongest Bragg reflections. Additional peaks were also evident in material formed during single-crystal growth. As a consequence of the modulated structure adopted by this compound (see below) we have not been able to unequivocally identify the impurity phase in this material. Nevertheless it was possible to fit the pattern for this sample in the tetragonal model in *P*4/*mmm*, with $a = 3.80981(2)$ and $c = 7.70132(4)$ Å, $R_p = 4.50\%$ and $R_{wp} = 6.50\%$, Figure 6. Attempts to refine a structure in *I*4/*mcm* that may occur if there was no Tm-vacancy ordering were unsuccessful; not only were the *R* factors unacceptably high ($R_p = 7.79\%$ and $R_{wp} = 14.11\%$), but this model did not predict the observed *X*-point reflections such as the 001 reflection at $d = 7.71$ Å ($2\theta \approx 4.4°$ at $\lambda = 0.60265$ Å).

To better understand the onset of the tetragonal structure in this material we investigated this using both electron and single-crystal X-ray diffraction. Both measurements showed incommensurate satellite reflections. Figure 7 shows a typical (a) [001] zone axis EDP of $Tm_{1/3}TaO_3$ and (b) the corresponding low-resolution lattice image. The three-index notation in Figure 7a is with respect to an $\mathbf{a} = \mathbf{a}_p + \mathbf{b}_p$, $\mathbf{b} = -\mathbf{a}_p + \mathbf{b}_p$, $\mathbf{c} = 2\mathbf{c}_p$ ($\mathbf{a}^* = {}^1/_2[110]_p^*$, $\mathbf{b}^* = {}^1/_2[-1,1,0]_p^*$, $\mathbf{c}^* = {}^1/_2[001]_p^*$) average substructure (labeled **G** hereafter). In addition to the strong Bragg reflections of the underlying perovskite substructure ($\mathbf{a}_p^* = [1,-1,0]^*$ and $\mathbf{b}_p^* = [110]^*$ and higher order linear combinations thereof) in Figure 7a, note the presence of a multitude of additional incommensurate satellite reflections at the $\mathbf{G} \pm m\varepsilon(\mathbf{a}^* - \mathbf{b}^*) \pm n\varepsilon(\mathbf{a}^* + \mathbf{b}^*)$ positions of reciprocal space, where *m* and *n* are integers and $\varepsilon = 0.079(1)$. Indexation with respect to the five basis vectors $\mathbf{a}^*$, $\mathbf{b}^*$, $\mathbf{c}^*$, $\mathbf{q}_1 = \varepsilon(\mathbf{a}^* - \mathbf{b}^*)$, and $\mathbf{q}_2 = \varepsilon(\mathbf{a}^* + \mathbf{b}^*)$ is also given in Figure 7a. Note the apparent condition $F(HK0MN0) = 0$ unless $H + K$ and $M + N$ are both even. The ~34.01 Å ($= {}^1/_2\varepsilon a^*$) crossed fringes in Figure 7b suggest some sort of checker-board type ordering pattern reminiscent of that recently reported by Guiton and Davies.[28] The regularity of this ordering pattern is apparent from the regularity of the lattice fringes in Figure 7b and the large number of high-order harmonics present in Figure 7a. Figure

(28) Guiton, B. S.; Davies, P. K. *Nat. Mater.* **2007**, *6*, 586.

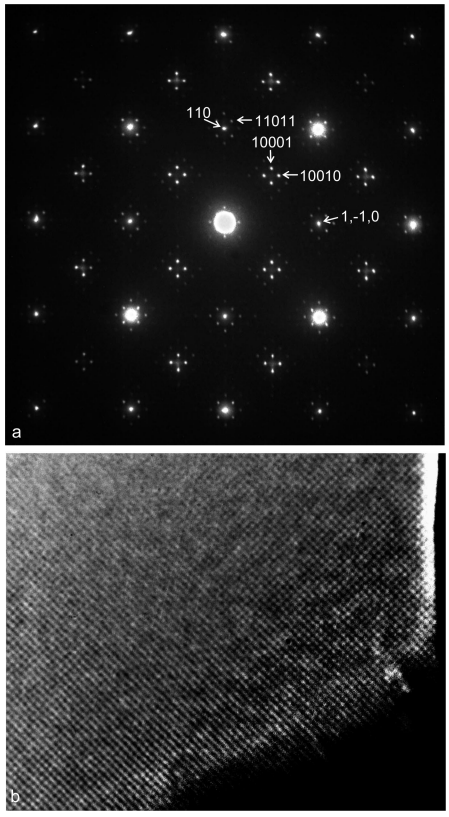

Figure 7. (a) Electron diffraction pattern of a [001] zone axis and (b) corresponding lattice image of $Tm_{1/3}TaO_3$.

8 shows the orthogonal (a) [$\bar{1}$10] and (b) [110] zone axis EDPs. The lack of diffuse streaks in the ⟨$\bar{1}$10⟩ zone reflects the transition from a disordered arrangement of the Ln cations seen in $Gd_{1/3}TaO_3$ to the modulated structure in $Tm_{1/3}TaO_3$. The presence of the incommensurate satellite reflections in all the illustrated EDPs points to complete ordering of the Tm cations within the layered structure, albeit in a very complex manner.

We now consider the evolution of the structures across the series. In general terms, tilting of the octahedra is expected to be accompanied by spontaneous lattice strains that lower the symmetry from cubic.[29] These spontaneous strains can be quantified by the anisotropy in the unit cell parameters and in the simplest case should increase as the tilt angle increases. Here we observe essentially zero spontaneous orthorhombic lattice strains in $Gd_{1/3}TaO_3$, suggesting the strain−tilting coupling has been suppressed. A similar effect was observed in $Ca_{1-x}Sr_xTiO_3$[29] where it was proposed that local (unit cell scale) strains develop around the dopant ions and that these frustrate the development of coherent, long-range relaxation of the cell. It is possible that local heterogeneities associated with the Gd-vacancy ordering could act in a similar manner, but given that all the $Ln_{1/3}TaO_3$ oxides exhibit very similar Ln-vacancy ordering this is clearly not the driving force for the minimization of the spontaneous strains.

It is probably not coincidental that the spontaneous strains are minimized just before the first-order *Cmmm*−*Pmma* transition that occurs as the Ln size is reduced from Gd [ionic radius 1.053 Å] to Tb [1.040 Å].[30] We have observed similar strain anomalies in the series $Sr_{2-x}A_xMWO_6$ (A = Ca, Ba, M = Co, Ni)[31,32] where the spontaneous strains are suppressed near the first-order *I*4/*m* to $P2_1/n$ transition. Like the *Cmmm*−*Pmma* transition, the *I*4/*m* to $P2_1/n$ transition involves a reorientation of the tilts.

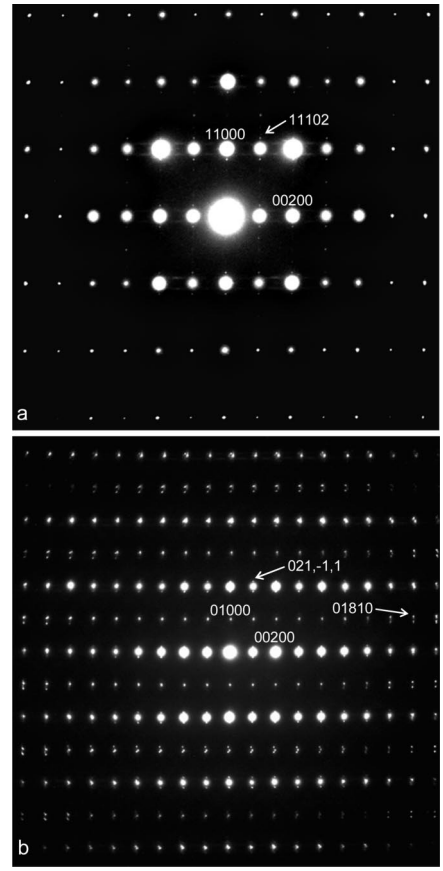

Figure 8. (a) [$\bar{1}$10] and (b) [110] zone axis electron diffraction patterns of $Tm_{1/3}TaO_3$.

In summary, analysis of the synchrotron patterns showed the sequence of phases in $Ln_{1/3}TaO_3$ to be as follows:

$$\underset{\text{tetragonal}}{P4/mmm} \rightarrow \underset{\text{orthorhombic}}{Cmmm} \rightarrow \underset{\text{orthorhombic}}{Pmma} \rightarrow \underset{\text{orthorhombic}}{Pmc2_1} \rightarrow \underset{\text{tetragonal}}{P4/mmm}$$

With the exception of the final transition to the tetragonal structure in $Tm_{1/3}TaO_3$ these structures represent a progressive reduction in symmetry associated with the decreasing size of the Ln cation.[30] The evolution of the reduced lattice parameters and volume across this series is illustrated in Figure 9, and the refined lattice parameters are tabulated in Table 3. It appears that the Tm cation is too small to occupy the A-type site and retain a commensurate structure, resulting in a transition to an incommensurate structure. On the basis of the group-theoretical analysis[12] the *P*4/*mmm* to *Cmmm* transition is allowed to be continuous, involving the intro-

(29) Carpenter, M. A.; Howard, C. J.; Knight, K. S.; Zhang, Z. M. *J. Phys.: Condens. Matter* **2006**, *18*, 10725.
(30) Shannon, R. D. *Acta Crystallogr., Sect. A* **1976**, *32*, 751.
(31) Zhou, Q. D.; Kennedy, B. J.; Elcombe, M. M. *J. Solid State Chem.* **2007**, *180*, 541.
(32) Zhou, Q. D.; Kennedy, B. J.; Howard, C. J.; Elcombe, M. M.; Studer, A. J. *Chem. Mater.* **2005**, *17*, 5357.

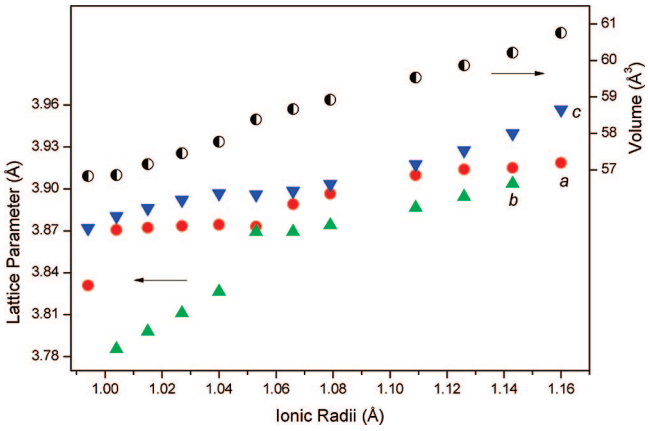

Figure 9. Summary of lattice parameters and volumes for the series $Ln_{1/3}TaO_3$. In this figure the values have been reduced to their equivalent in the primitive cubic cell. The parameters in *Pmma* and *Pmc*2_1 are presented using the nonstandard settings as listed in Table 3. Where not apparent the estimated standard deviations (esd's) are smaller than the symbols.

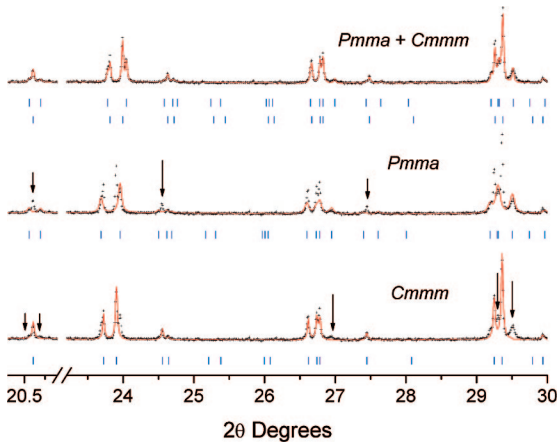

Figure 10. Portion of the synchrotron diffraction pattern for $Tb_{0.6}Gd_{0.4}Ta_3O_9$ demonstrating the coexistence of the *Pmma* and *Cmmm* phases. In all traces, the observed data are shown by the crosses and the solid line is the result of fitting by the stated model. The shortest vertical lines show the positions of the space group allowed Bragg reflections. The data were collected at λ = 0.80155 Å at the Australian synchrotron.

duction of out-of-phase tilting about the 100 axis. The *Cmmm*−*Pmma* transition involves a reorientation of the tilts from [100] to [110], and such a transition must be first order. Finally the *Pmma*−*Pmc*2_1 transition introduces additional tilting about [001] and may be continuous. A *Pmc*2_1−*P*4/*mmm* transition is unexpected since it involves the simultaneous loss of these two unequal tilts.

Solid Solutions. Above we showed that reducing the size of the lanthanide cation induces two first-order phase transitions, *Cmmm* to *Pmma* near r_{Ln}1.05 Å [Ln = Gd−Tb] and *Pmc*2_1 to *P*4/*mmm* r_{Ln}1.00 Å [Ln = Er−Tm]. To further probe these two transitions a number of members of the solid solutions $Tb_{(1-x)/3}Gd_{x/3}TaO_3$ and $Tm_{(1-x)/3}Er_{x/3}TaO_3$ were also prepared and structurally characterized. The diffraction patterns of the four members of the series $Tb_{(1-x)/3}Gd_{x/3}TaO_3$ were not well fitted to a single-phase model in either *Cmmm* or *Pmma* but, rather, consisted of two phases, one in *Cmmm* and one in *Pmma*, see Figure 10. In the refinements of the two-phase model, the positions of the anions were fixed at those found for the single-phase end-members and the profile

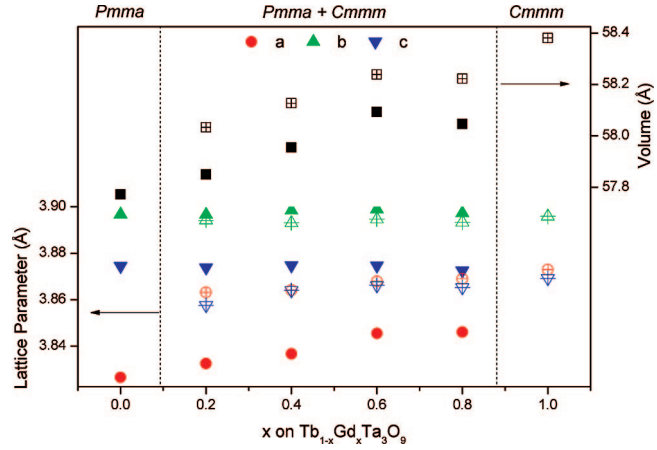

Figure 11. Variation of the lattice parameters for the solid solutions $Tb_{(1-x)/3}Gd_{x/3}TaO_3$ expressed as $Tb_{1-x}Gd_xTa_3O_9$. The open symbols are for the *Cmmm* phase, and the closed symbols are for the *Pmma* phase. The circles represent the *a*-parameter, the up triangle represents the *b*-parameter, and the down triangle represents the *c*-parameter. The squares are the volumes.

parameters were constrained to be equal for the two phases. Although complete solubility was not, apparently, obtained, we did observe (Figure 11) a systematic increase in the volume of the two phases upon doping with Gd, suggesting the coexistence of the two phases is related to the nature of the phase transition. It is important to note that the phase composition does not show a linear dependence on the elemental composition, see Table 5, confirming that solid solutions were in fact formed and that phase separation has occurred.

Adding ~20% Tm to $Er_{1/3}TaO_3$ results in the formation ~56% tetragonal *P*4/*mmm* and ~44% orthorhombic *Pmc*21 phases (see Table 6). Doping to 60% yields a single-phase tetragonal material, Figure 12. Evidently in this case the progressive introduction of the smaller Tm cation induces the transition to the tetragonal phase. It was evident from the results for the single lanthanide containing $Ln_{1/3}TaO_3$ samples that Tm is too small to occupy the 2*a* site in *Pmc*2_1. Rather this exhibits a tetragonal structure with a complex modulation. Evidently even a small reduction in the effective size of the A-site cation is sufficient to induce the transition to tetragonal. It remains to be established if the phase separation identified here is related to the nanochessboard superlattices reported recently by Guiton and Davies[28] in $(Nd_{2/3-x}Li_{3x})TiO_3$. These authors argued that the complex behavior stems from differences in the bonding preferences of the two A-site cations, although in this case the complex structure exists in the absence of doping.

Variable-Temperature Studies. Heating a sample of $Nd_{1/3}TaO_3$ results in a progressive reduction in the magnitude of the orthorhombic splitting, and at 500 °C the structure appears to be tetragonal. The temperature dependence of the lattice parameters indicates that the orthorhombic to tetragonal transition is continuous, Figure 13. The refined structural parameters for $Nd_{1/3}TaO_3$ in both phases are listed in Table 7.

It is evident from Figure 13 that the volume of the orthorhombic phase is somewhat reduced from that estimated by extrapolation from the volume of the high-temperature tetragonal phase. This reflects the presence of spontaneous

Table 5. Summary of the Rietveld Refinements for $Tb_{1-x}Gd_xTa_3O_9$ Illustrating the Progressive Increase in the *Cmmm* Phase with Increasing Gd Content[a]

	Cmmm		*Pmma*		*Pmma* + *Cmmm*		two-phase ratio	
	R_p	R_{wp}	R_p	R_{wp}	R_p	R_{wp}	*Cmmm* wt %	*Pmma* wt %
$Tb_{0.8}Gd_{0.2}$	7.36	11.37	4.27	5.66	**3.94**	**5.14**	15	85
$Tb_{0.6}Gd_{0.4}$	5.40	7.71	5.49	7.79	**4.28**	**5.49**	64	36
$Tb_{0.4}Gd_{0.6}$	4.28	5.57	4.28	5.57	**3.84**	**4.86**	80	20
$Tb_{0.2}Gd_{0.8}$	4.31	5.68	4.49	5.96	**4.05**	**5.19**	91	9

[a] Both end-member samples were single phase. The best fits are indicated by the bold entries.

Table 6. Summary of the Rietveld Refinements for $Tm_{1-x}Er_xTa_3O_9$ Illustrating the Progressive Increase in the *Cmmm* Phase with Increasing Er Content[a]

	P4/mmm		*Pmc*2_1		*P4/mmm* + *Pmc*2_1		phase composition	
	R_p	R_{wp}	R_p	R_{wp}	R_p	R_{wp}	*P4/mmm* wt %	*Pmc*2_1 wt %
$Tm_{0.8}Er_{0.2}$	3.76	4.96					100	0
$Tm_{0.6}Er_{0.4}$	5.80	7.62					100	0
$Tm_{0.4}Er_{0.6}$	4.49	6.22	4.45	5.91	**4.30**	**5.77**	88	12
$Tm_{0.2}Er_{0.8}$	5.66	8.58	5.40	7.98	**3.75**	**4.86**	56	44

[a] Both end-member samples were single phase. The best fits are indicated by the bold entries.

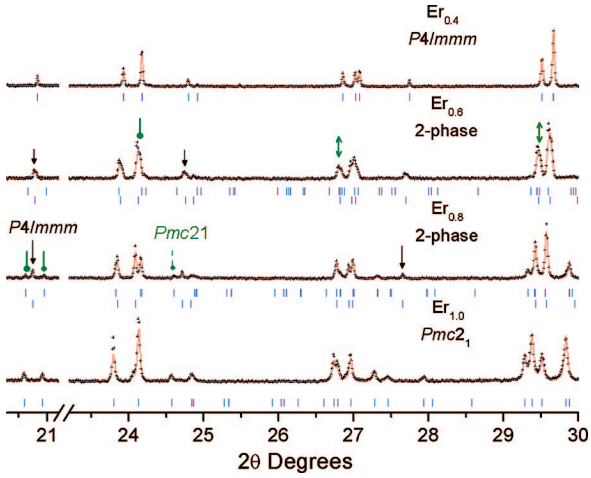

Figure 12. Portion of the synchrotron diffraction pattern for members in the series $Er_{1-x}Tm_xTa_3O_9$ demonstrating the evolution from *Pmc*2_1 to *P4/mmm*. In all traces, the observed data are shown by the crosses and the solid line is the result of fitting by the stated model. The shortest vertical lines show the positions of the space group allowed Bragg reflections. The data were collected at $\lambda = 0.80155$ Å.

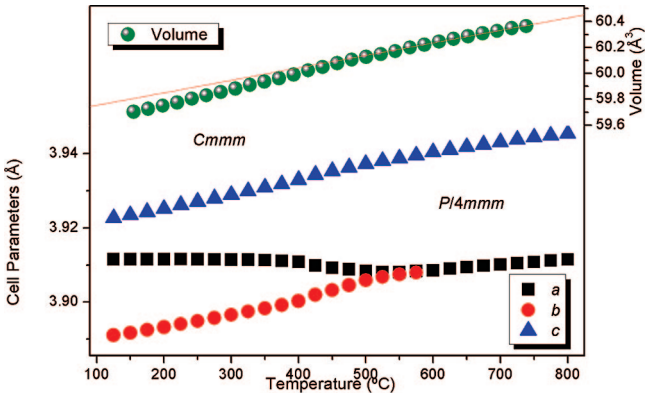

Figure 13. Temperature dependence of the lattice parameters and volume for $Nd_{1/3}TaO_3$ illustrating the continuous transition from *Cmmm* to *P4/mmm*. Where not apparent the esd's are smaller than the symbols.

strains within the structure. The nature of the transition can be established by examination of the temperature dependence of an appropriate order parameter. The orthorhombic strain is proportional to the square of the order parameter and a plot of $e_{ortho}{}^2$ versus temperature is linear as required for a

Table 7. Refined Lattice and Positional Parameters for $Nd_{1/3}TaO_3$ in Both the Orthorhombic (Room Temperature) and Tetragonal (550 °C) Phases

atom	site	*x*	*y*	*z*	B_{iso}
Room Temperature, $a = 7.81849(6)$, $b = 7.77200(6)$, $c = 7.83380(7)$ Å					
Nd	4*g*	0.2470(17)	0	0	0.11(3)
Ta	8*n*	0	0.2503(13)	0.2596(1)	−0.02(2)
O1	4*i*	0	0.2789(36)	0	0.41(12)[a]
O2	4*j*	0	0.2196(34)	0.5	0.41(12)
O3	4*k*	0	0	0.2037(29)	0.41(12)
O4	4*l*	0	0.5	0.2608(35)	0.41(12)
O5	8*m*	0.25	0.25	0.2268(16)	0.41(12)
$T = 550$ °C, $a = 3.90720(3)$, $c = 7.87641(6)$ Å					
Nd	1*c*	0.5	0.5	0	0.89(3)
Ta	2*g*	0	0	0.2598(1)	0.61(2)
O1	1*a*	0	0	0	2.28(15)[a]
O2	1*b*	0	0	0.5	2.28(15)
O3	4*i*	0	0.5	0.2325(18)	2.28(15)

[a] In these, and all other refinements using synchrotron diffraction data, the displacements of the anions were constrained to be equal.

tricritical transition. From this the transition temperature is estimated to be 500 °C as well. A high-resolution powder neutron diffraction study of $Nd_{1/3}NbO_3$ demonstrated[14] that this also undergoes a continuous transition from *Cmmm* to *P4/mmm*, albeit at slightly higher temperature of ~650 °C. In this case it was demonstrated that the orthorhombic to tetragonal transition is driven by the disappearance of the octahedral tilting. Neutron diffraction measurements of $Nd_{1/3}TaO_3$ would be required to verify this.

That $Gd_{1/3}TaO_3$ is orthorhombic in *Cmmm* was demonstrated by synchrotron X-ray diffraction and electron diffraction. Heating the sample to 800 °C did not result in any obvious change in the appearance of the synchrotron X-ray diffraction pattern, suggesting the structure remains in the same space group over this temperature range. Refinements in *Cmmm* were successful for all temperatures investigated. The persistence of the orthorhombic structure in $Gd_{1/3}TaO_3$ is in marked contrast to that observed for $Nd_{1/3}TaO_3$ where the orthorhombic splitting is progressively reduced as the temperature was increased, ultimately becoming tetragonal. The existence of the metrically tetragonal, but strictly orthorhombic, structure in $Gd_{1/3}TaO_3$ is, as noted above, similar to the observation of a metrically cubic, but strictly orthorhombic, phase in $Ca_{1-x}Sr_xTiO_3$[29] and metrically cubic

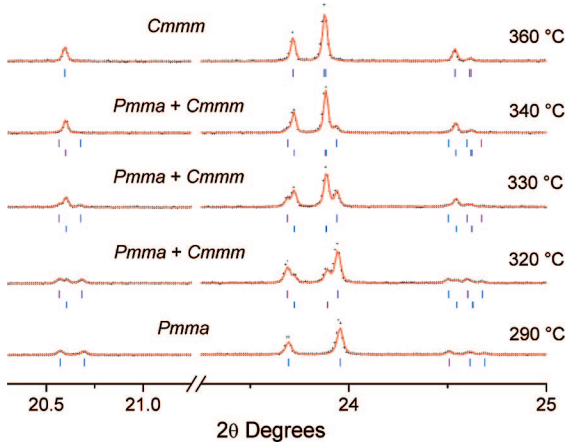

Figure 14. Portion of the synchrotron diffraction pattern for $Tb_{1/3}TaO_3$ at the listed temperatures demonstrating the coexistence of the *Pmma* and *Cmmm* phases between 320 and 340 °C. In all traces, the observed data are shown by the crosses and the solid line is the result of fitting by the stated model. The shortest vertical lines show the positions of the space group allowed Bragg reflections. The data were collected at $\lambda = 0.80073$ Å.

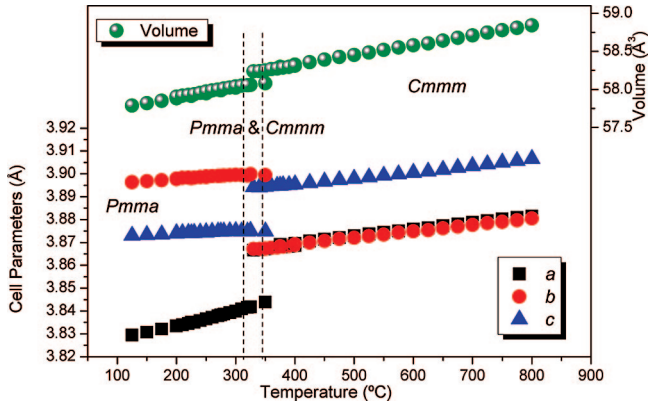

Figure 15. Temperature dependence of the lattice parameters for $Tb_{1/3}TaO_3$ illustrating the first-order transition from *Pmma* to *Cmmm*. Where not apparent the esd's are smaller than the symbols.

but monoclinic phase in $Sr_{2-x}A_xNiWO_6$[32] and $Sr_{2-x}A_x$-$CoWO_6$[31] It appears that close to the tolerance factor limit that triggers the first-order transition, the lattice distortions that can be described by the spontaneous strains become minimized. It is possible that this corresponds to a form of preordering of the structure prior to the phase transition. It is remarkable that this high-pseudosymmetry structure persists over such a large temperature range. A similar effect is observed for $Sr_{2-x}A_xNiWO_6$[32] where heating over a similar temperature range has very little effect on the magnitude of the strains.

Heating a sample of $Tb_{1/3}TaO_3$ shows an abrupt dramatic change in appearance near 320 °C, from a pattern that is clearly orthorhombic at 290 °C to one that is apparently tetragonal at 360 °C, see Figure 14. This change is accompanied by a small but noticeable increase in the cell volume (Figure 15). Examination of the diffraction pattern showed the diagnostic *Pmma* doublet near $2\theta \approx 20.6°$ ($d \approx 2.34$ Å) becomes a singlet near 360 °C, Figure 14. Careful examination of the diffraction patterns indicates that the structure in the high-temperature phase is orthorhombic and in *Cmmm*. A transition between *Cmmm* ($a^-b^0c^0$) and *Pmma* ($a^-a^-c^0$) involves a reorientation of the tilts, and as noted above, the group-theoretical analysis shows this must be first order.

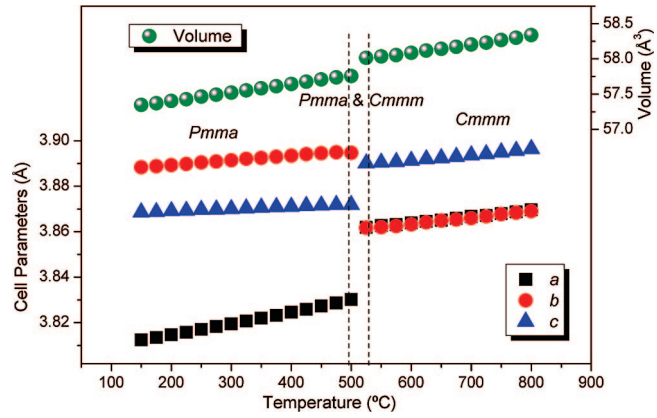

Figure 16. Temperature dependence of the lattice parameters for $Dy_{1/3}TaO_3$ illustrating the first-order transition from *Pmma* to *Cmmm*. Where not apparent the esd's are smaller than the symbols.

During the structural analysis it was noted that the patterns recorded at or below 300 °C were well fitted to a single-phase model in *Pmma*, and those recorded at or above 360 °C were well fitted to a single-phase model in *Cmmm*. In the intermediate temperature region the patterns were noticeably more complex (Figure 14), and satisfactory fits required the use of a two-phase (*Pmma* and *Cmmm*) model. The coexistence of these two phases is not unexpected given the first-order nature of the transition between them and is similar to that seen in the solid solutions.

The temperature dependence of the structure of $Dy_{1/3}TaO_3$ is very similar to that of $Tb_{1/3}TaO_3$ with the first-order *Pmma*−*Cmmm* transition occurring at slightly higher temperature of ≈525 °C (cf. ≈360 °C), see Figure 16. This is consistent with the smaller Dy inducing a larger distortion of the lattice. Again we see evidence for the coexistence of the *Pmma* and *Cmmm* phases over a limited temperature range.

The diffraction pattern of $Tm_{1/3}TaO_3$ showed no significant changes upon heating to 800 °C. The long-range structure clearly remains tetragonal over this temperature range with a systematic increase in the cell volume being noted, Figure 17.

Concluding Remarks. Finally we turn to differences between the present $Ln_{1/3}TaO_3$ and $Ln_{1/3}NbO_3$[14,15] oxides and the $Ln_{2/3}TiO_3$ oxides.[12,13] The most obvious difference is that the former contains one-third A-site cations and the latter one-third vacancies, but both with layered ordering of the A-site cations/vacancies along the *z*-axis. The tantalates adopt a $Pmc2_1$ ($a^-a^-c^+$) orthorhombic structure, whereas the titanates apparently favor a $C2/m$ ($a^-b^0c^-$) monoclinic structure. Apparently, having more cations at the A-site favors the latter. Whereas the $C2/m$ monoclinic structure can be obtained by a continuous transition from *Cmmm*, the primitive orthorhombic structure ($Pmc2_1$) can only be obtained by a continuous transition from the $\sqrt{2} \times 2 \times \sqrt{2}$ *Pmma* structure. It is possible that this reflects an electrostatic effect associated with the cation ordering. Recall that in general the tilt system displayed by $A^{2+}B^{4+}O_3$ and $A^{3+}B^{3+}O_3$ perovskites is different with the former favoring

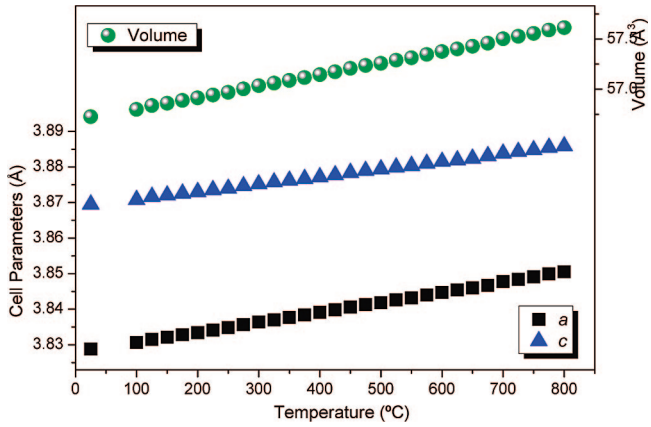

Figure 17. Temperature dependence of the lattice parameters for $Tm_{1/3}TaO_3$ established from the synchrotron X-ray powder diffraction. The lattice parameters were estimated using *P4/mmm*. Where not apparent the esd's are smaller than the symbols.

a single tilt about [001] ($a^0a^0c^-$), whereas the latter favors a tilt around [111] ($a^-a^-a^-$).

In conclusion, we have established that the structures in the series $Ln_{1/3}TaO_3$ evolve as follows:

$$\frac{P4/mmm}{a^0a^0c^0} \rightarrow \frac{Cmmm}{a^-b^0c^0} \rightarrow \frac{Pmma}{a^-a^-c^0} \rightarrow \frac{Pmc2_1}{a^-a^-c^+} \rightarrow \frac{P4/mmm}{a^0a^0c^0}$$

Near the *Cmmm*−*Pmma* transition, the *Cmmm* phase is characterized by high pseudosymmetry, appearing as metrically tetragonal in $Gd_{1/3}TaO_3$. The high pseudosymmetry is due to suppression of the strain−order-parameter coupling, a phenomenon that has been observed in a number of other perovskite[25,31−33] and nonperovskite materials.[34] Indeed earlier workers[1−4] had mistakenly described the structure of $Gd_{1/3}TaO_3$ as being tetragonal; the combined X-ray and electron diffraction studies demonstrate it to be orthorhombic. The *Cmmm* phase is also observed, at elevated temperature, in $Tb_{1/3}TaO_3$ and $Dy_{1/3}TaO_3$. In both cases it is found to be pseudotetragonal.

That we find $Tm_{1/3}TaO_3$ is tetragonal is surprising, but it is consistent with earlier reports. The electron diffraction studies, however, show that this is not a simple structure. The bulk structure as determined using synchrotron X-ray diffraction shows this has A-type cation/vacancy ordering, and clearly the transition to tetragonal is not a consequence of cation disorder. Recall that only the largest lanthanides [Ln—La, Pr, Nd] form the analogous Nb oxides $Ln_{1/3}NbO_3$ using conventional solid-state methods,[14,15] suggesting that below a critical size these $Ln_{1/3}NbO_3$ perovskites cannot be formed. $Tm_{1/3}TaO_3$ appears to be at the limit, and the material forms via a complex local ordering of the cations (in addition to the layered ordering of the A-site cations/vacancies along the *z*-axis). Future work aimed at better characterizing these phase transitions using high-resolution neutron diffraction is planned and will be reported in due course.

Acknowledgment. This work has been partially supported by the Australian Research Council and the Australian Institute of Nuclear Science and Engineering (AINSE) through the provision of AINSE Postgraduate Awards to Paul Saines and Neeraj Sharma. The work performed at the Australian National Beamline Facility (ANBF) was supported by the Australian Synchrotron Research Program, which is funded by the Commonwealth of Australia under the Major National Research Facilities program. The assistance of Dr. Yoshiki Kubota with the synchrotron radiation experiments performed at BL02B2 in the SPring-8 Japan Synchrotron Radiation Research Institute (JASRI) (Proposal No. 2007A1875) is gratefully acknowledged. We thank Dr. Rene Macquart for guidance on the use of the floating zone furnace and Dr. Chris Howard for numerous illuminating discussions regarding structures of perovskites.

CM8014868

(33) Carpenter, M. A.; Howard, C. J.; Knight, K. S.; Zhang, Z. M. *J. Phys.: Condens. Matter* **2006**, *18*, 10725.
(34) Carpenter, M. A. In *Transformation Processes in Minerals*, 2000; Vol. 39, p 35.